



# Ultra-ductile behavior of fly ash-based engineered geopolymer composites with a tensile strain capacity up to 13.7%

Huy Hoàng Nguyễn<sup>a</sup>, Quang-Hiếu Lương<sup>a</sup>, Jeong-Il Choi<sup>b</sup>, Ravi Ranade<sup>c</sup>, Victor C. Li<sup>d</sup>,  
Bang Yeon Lee<sup>a,e,\*</sup>

<sup>a</sup> Department of Architecture and Civil Engineering, Chonnam National University, Gwangju 61186, Republic of Korea

<sup>b</sup> Biohousing Research Center, Chonnam National University, Gwangju 61186, Republic of Korea

<sup>c</sup> Department of Civil, Structural, and Environmental Engineering, University at Buffalo, State University of New York, 135 Ketter Hall, Buffalo, NY 14260-4300, USA

<sup>d</sup> Department of Civil and Environmental Engineering, University of Michigan, MI 48109-2125, USA

<sup>e</sup> School of Architecture, Chonnam National University, Gwangju 61186, Republic of Korea

## ARTICLE INFO

### Keywords:

Fly ash  
Geopolymer  
Composite  
Tensile strain capacity  
Micromechanics

## ABSTRACT

This study introduces ultra-ductile fly ash-based engineered geopolymer composites (UD-EGCs). Four mixtures of UD-EGCs with different ratios of sodium metasilicate pentahydrate (SMP)-to-sodium hydroxide (SH) were designed and prepared at an identical water-to-binder ratio. Polyethylene (PE) fibers at 1.75 vol% were used as reinforcements. Experimental and analytical investigations of mechanical properties, micromechanical analysis, and chemical characterization of UD-EGCs were performed at both meso- and micro-scales. The UD-EGC mixtures were found to strain-harden with ultra-high ductility. Notably, the mixture using an SMP/SH ratio of 1.5 achieved a tensile strain capacity of 13.7% and a tensile strength of 6.8 MPa. Moreover, all mixtures were lightweight, with density below 1.83 g/cm<sup>3</sup>. From the chemical analysis, C-(N)-A-S-H and N-A-S-H were verified as the primary geopolymeric products of fly ash-based engineered geopolymer composites.

## 1. Introduction

For the last three decades, extensive research has been conducted on engineered cementitious composites (ECCs) – a class of fiber-reinforced cementitious composites possessing excellent tensile ductility. Unlike normal concrete, ECCs exhibit pseudo strain-hardening behavior and multiple-cracking phenomena [1]. Using micromechanical design theory, the crack width of ECC is inherently controlled, commonly below 100 μm [2]. As a result, ECC materials have much potential for enhancing the infrastructure durability [3]. Moreover, due to its superior tensile strain capacity, which is several hundreds of times higher than that of normal concrete, ECC can be used for structures subjected to extreme loads due to natural (earthquake, hurricane, tsunami, etc.) or man-made disasters (terrorism, explosion, collision, etc.). However, ECC materials have certain limitations. For example, these materials utilize a low water-to-binder (*w/b*) ratio, commonly in the range of 0.2 to 0.3 [4], which necessitates the use of a large amount of ordinary Portland cement (OPC). The manufacture of OPC releases a considerable amount of CO<sub>2</sub> into the atmosphere, contributing to environmental pollution and exacerbating the greenhouse effect [5–8]. These are issues that need to

be tackled urgently [9]. Environmental degradation is exacerbated when the use of natural resources is unsustainable; therefore, resource efficiency has an important impact on environmental degradation. The problems of both resource efficiency and environmental degradation in the construction materials industry should not be underplayed. For example, in its manufacturing process, OPC consumes a disproportionately high volume of raw materials and energy, and produces a lot of CO<sub>2</sub>. Around 8% of all CO<sub>2</sub> emission comes from cement production [10, 11]. The construction industry only continues to grow, which means that the demand for OPC supply is constantly increasing, and the source materials used in OPC production will be exhausted in the not too distant future [12]. Thus, using more eco-friendly or recycled construction materials in a sustainable manner is key to improving resource efficiency and reducing environmental degradation.

In an effort to address this limitation, a new class of cement-free inorganic binders named geopolymers has been developed to replace OPC. Originally developed by Kuhl [13,14], geopolymers are eco-friendly and sustainable inorganic binders, combining pozzolanic materials (fly ash, slag, metakaolin, etc.) and alkali activators. As reported in the literature, one-part geopolymers yielded less than 10% of

\* Corresponding author.

E-mail address: [bylee@jnu.ac.kr](mailto:bylee@jnu.ac.kr) (B.Y. Lee).

<https://doi.org/10.1016/j.cemconcomp.2021.104133>

Received 18 April 2021; Received in revised form 31 May 2021; Accepted 2 June 2021

Available online 8 June 2021

0958-9465/© 2021 Elsevier Ltd. All rights reserved.

**Table 1**  
Mix proportions of UD-EGC (weight ratios of binder).

Mix ID	Binder			Water	SP	VMA	Defoamer	Fiber (vol%)
	Fly ash	SH	SMP					
UD-EGC10	0.80	0.10	0.10	0.345	0.009	0.001	0.001	1.75
UD-EGC15	0.75	0.10	0.15	0.345	0.003	0.001	0.001	
UD-EGC20	0.70	0.10	0.20	0.345	0.003	0.001	0.001	
UD-EGC25	0.65	0.10	0.25	0.345	–	0.005	0.001	

global warming potential compared with OPC-based mixtures [15]. Different from the hydration process of OPC, geopolymer synthesis basically involves a sequence of processes, including dissolution, speciation equilibrium, gelation, reorganization, polymerization, and condensation [16]. Notably, thermal curing, i.e., heat curing or steam curing, is essential to speed up the geopolymerization [17]. Therefore, geopolymers are more appropriate for the fabrication of precast structures than for on-site construction [16,18]. As reported, the mechanical properties of geopolymer concrete are similar to those of normal concrete, or even higher in certain cases [19]. Especially, geopolymer concrete is commonly used as fire-resistant construction material or for building structures exposed to toxic and corrosive environments not tolerated by traditional concrete [20].

Based on the micromechanical design basis of ECC, strain-hardening fiber-reinforced engineered geopolymer composites (SH-EGC) have been developed recently from a variety of aluminosilicate source materials, alkali activators, and short polymeric fibers [21]. Both metallic and polymeric fibers have been used for reinforcing SH-EGC. Steel fibers possessing high elastic modulus and tensile strength have been used to obtain high strength SH-EGC [22,23]. On the other hand, hydrophilic polyvinyl alcohol (PVA) fibers with lower elastic modulus and tensile strength than steel fibers have been used to achieve high tensile ductility of SH-EGC [24,25]. Polyethylene (PE) fibers are hydrophobic polymeric fibers whose tensile strength is approximately two times higher than that of the PVA fibers, and the elastic modulus of the PE fibers is half that of steel fibers. PE fibers have been used to achieve a SH-EGC with both high strength and high ductility [7,24].

Overall, SH-EGCs using PE fibers are capable of achieving tensile properties as good as those of ECCs. Nematollahi et al. (2016) investigated the micromechanics of high-ductile PE fiber-reinforced one-part slag/fly ash blended geopolymer composites, achieving tensile strain capacity up to 5.5% and tensile strength of 4.6 MPa [26]. Later, Choi et al. (2016) developed PE fiber-reinforced alkali-activated slag composites with ultra-high tensile strain capacity of 7.5% and tensile strength of 13.1 MPa [7]. Shaikh et al. (2018) reported tensile strain capacity up to 6% and tensile strength of over 4 MPa for a PE-fiber-reinforced conventional (two-part) slag/fly ash blended-based composites [27]. Interestingly, Yu and co-workers [28–32] proposed a new class of ultra-high-performance ECC (UHP-ECC) reinforced by PE fibers, with a remarkable tensile strain capacity of up to 12% and a tensile strength of up to 17 MPa, representing a tensile performance far superior to those of SH-EGCs.

In the present paper, a new class of PE fiber-reinforced fly ash-based ultra-ductile engineered geopolymer composites (UD-EGC) were developed employing a new technique based on the dissolution of sodium silicate pentahydrate particles into sodium hydroxide solution. The UD-EGC was optimized using different sodium silicate pentahydrate/sodium hydroxide ratios. At the meso-scale, the tensile behavior of UD-EGC was evaluated using direct tension tests. At the micro-scale, a micromechanics-based investigation via single fiber pull-out tests was

**Table 2**  
Chemical composition of fly ash (%).

SiO <sub>2</sub>	Al <sub>2</sub> O <sub>3</sub>	CaO	Fe <sub>2</sub> O <sub>3</sub>	Na <sub>2</sub> O	K <sub>2</sub> O	MgO	SO <sub>3</sub>	TiO <sub>2</sub>	Other
74.59	14.38	3.02	2.75	1.77	0.82	0.75	0.69	0.70	0.53

**Table 3**  
Physical properties of PE fiber.

Diameter (μm)	Length (mm)	Tensile strength (MPa)	Density (g/cm <sup>3</sup> )	Elastic modulus (GPa)
12	18	2700	0.97	88

performed to characterize the fiber-matrix bond properties of UD-EGC. The results were implemented in fiber-bridging analyses to investigate the fiber bridging behavior of UD-EGC. The morphology and chemical composition of the UD-EGC matrix were studied using scanning electron microscopy (SEM) and energy-dispersive X-ray spectroscopy (EDS) techniques.

## 2. Materials and experimental methods

### 2.1. Materials and mix proportions

Table 1 lists the mix designs investigated in the present study. The *w/b* ratio was 0.345 for all mixtures. Fly ash was the main source of aluminosilicate. The chemical compositions of fly ash, as determined by X-ray fluorescence (XRF) analysis, are listed in Table 2. The fly ash was activated by alkali activators comprising sodium metasilicate pentahydrate (SMP) powder and sodium hydroxide (SH) solution, which has not been previously reported in the literature. Because SMP is water-based, it can be dissolved in an aqueous solution at elevated temperature. Specifically, the technique to prepare the alkali solution was based on three successive steps. First, crystalline flakes of SH were added to water to obtain the SH solution with a specific molar concentration of 7.2 M. The dissolution of SH is a highly exothermic process. Second, fine SMP powder was introduced into the hot SH solution, which was stirred well for 5 min to ensure complete dissolution of SMP. Finally, the sodium-based liquid activator was cooled for an additional 30 min before mixing with fly ash and other constituents of UD-EGC.

A superplasticizer (SP) and a viscosity modifying admixture (VMA) were used to control the viscosity of the matrix materials and ensure a good fiber dispersion. The SP was a polycarboxylate-based superplasticizer, and the VMA was methylcellulose (C<sub>6</sub>H<sub>7</sub>O<sub>2</sub>(OH)<sub>x</sub>(OCH<sub>3</sub>)<sub>y</sub>). In addition, a defoamer based on mineral substances without silicone was used to minimize the air bubbles created during the mixing process. The PE fibers with high tensile strength and elastic modulus were added at the end. Table 3 lists the physical properties of the PE fiber.

### 2.2. Specimen preparation

Fly ash and sodium-based alkali-activator solution were mixed in a planetary mixer for 2 min at 90 revolutions per minute (rpm) and for another 3 min at 180 rpm. SP, VMA, and defoamer were then added to the mixture to achieve a rheology favorable for good fiber dispersion

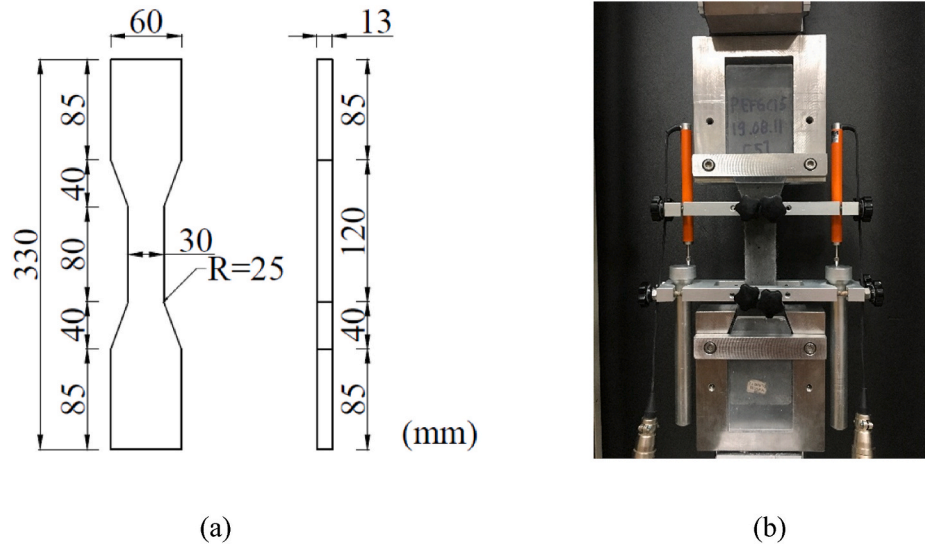


Fig. 1. (a) Specimen geometry and (b) tension test setup.

and to prevent unintentional air bubbles during mixing. Subsequently, the PE fibers were slowly introduced into the mixture. Then, the mixing procedure was continued for an additional 5 min at a relatively high speed of 270 rpm. When mixing was completed, the fresh mixture was poured into molds (three 50-mm cubes for the cube compression test and three dumbbell-shaped specimens for the uniaxial tension test). For the micromechanical tests, the same mixture without PE fibers was prepared, and the mixture was cast into three single fiber pullout molds and three prismatic beam molds with pre-existing notch. All the specimens were removed from the molds after curing for five days in air at  $23\text{ }^{\circ}\text{C} \pm 3\text{ }^{\circ}\text{C}$ , and were then placed in an oven at  $80\text{ }^{\circ}\text{C}$  for 36 h. The hardened specimens were subsequently placed in a curing chamber at  $23\text{ }^{\circ}\text{C} \pm 3\text{ }^{\circ}\text{C}$  until 28 days of age.

### 2.3. Density and mechanical tests

The hardened density ( $\rho_h$ ) of UD-EGC mixtures was measured using the weight of 50-mm cube specimens at 28 days of age, according to the following equation:

$$\rho_h = \frac{w_a}{w_a - w_b} \times \rho_w \quad (1)$$

where  $w_a$  and  $w_b$  were the weights of cube specimens in air and in water, respectively.  $\rho_w$  was the density of water, equal to  $1\text{ g/cm}^3$ . It should be noted that  $w_a$  was obtained in a surface-dried condition, while  $w_b$  was measured in a state of complete water immersion. The compressive strength ( $f_c$ ) of cube specimens was determined in accordance with ASTM C109 [33].

Tensile specimens with dumbbell shape were adopted to evaluate the tensile performance. Specifically, uniaxial tension tests were performed in universal tensile testing machine according to the recommendations of the Japan Society of Civil Engineers (JSCE) [34]. Fig. 1 shows the specimen geometry with specific dimensions and the uniaxial test setup. The tensile load was applied to specimens at a loading rate of 0.1 mm/min. Two linear variable differential transducers were attached to either sides of the tensile specimen to measure the elongation within the

gauge length (80 mm). After the tension tests, the number of cracks within the gauge length for each specimen was counted manually using a magnifier. The average crack spacing was calculated by dividing the gauge length by the number of cracks. From the assumption that all deformations occurred at the cracks (i.e. elastic deformation of the uncracked matrix was negligible compared to the crack openings), the average crack width was calculated by dividing the elongation at ultimate tensile strength of each specimen by the number of cracks.

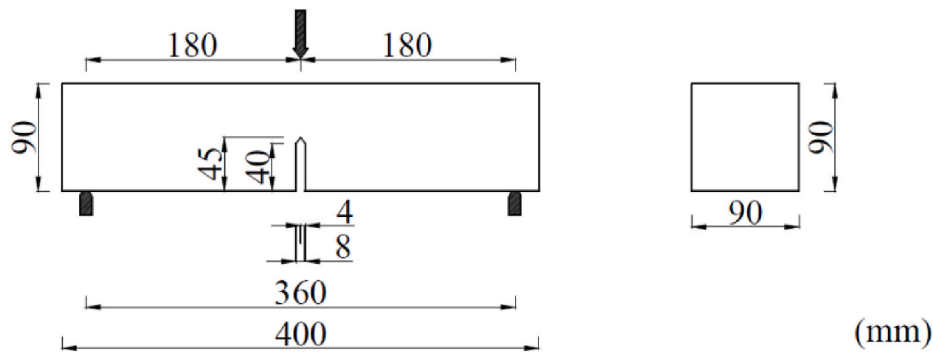
### 2.4. Matrix fracture toughness and single fiber pullout tests

As specified in ASTM E399 [35], a notched prism beam was adopted to measure the fracture toughness of the matrix. Fig. 2 shows the dimensions of the notched beam and the test configuration. A notch with depth of 45 mm was artificially generated on the beam by removing a plastic piece placed in the mold during casting specimens.

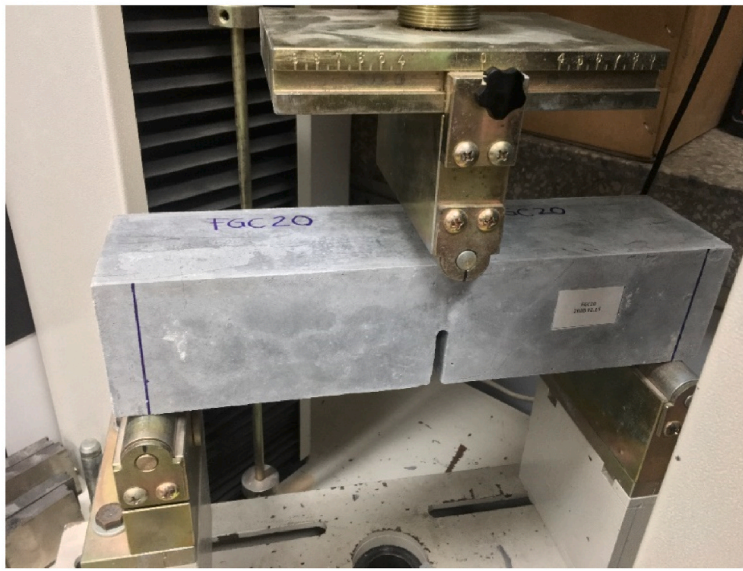
For the single fiber pullout tests, a single PE fiber was embedded into the matrix with an embedded length of 3 mm. The specimen dimensions and the test setup of the fiber pullout test are shown in Fig. 3. The bottom of the specimen was fixed to an aluminum plate, whereas the free-end of the fiber was gently affixed to an acrylic plate. The fiber pullout test was performed following Radon et al. (2001) [36]. Specifically, a load cell (load capacity: 5 N) and a laser displacement sensor were used to measure the pullout load and the pullout distance of fibers, respectively. The load was applied at a displacement rate of  $10\text{ }\mu\text{m/s}$ .

### 2.5. Chemical analysis

At micro-scale, the hydration products of UD-EGC were characterized based on SEM and EDS analysis. Specifically, a sample with volume smaller than  $1\text{ cm}^3$  detached from the tensile specimen was vacuumed and covered with palladium before testing. An SEM using secondary electron imaging mode and an EDS based on X-ray elemental mapping were adopted to investigate the morphology and to perform chemical analysis.



(a)



(b)

Fig. 2. Fracture toughness test showing (a) specimen configuration and (b) test set-up.

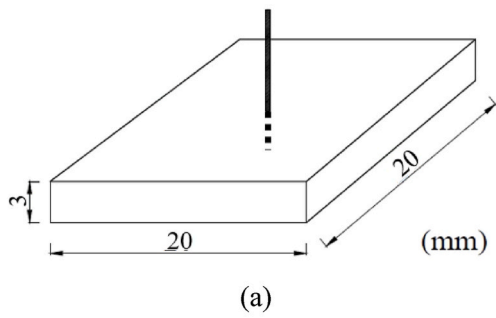
### 3. Results and discussion

#### 3.1. Compressive strength and density

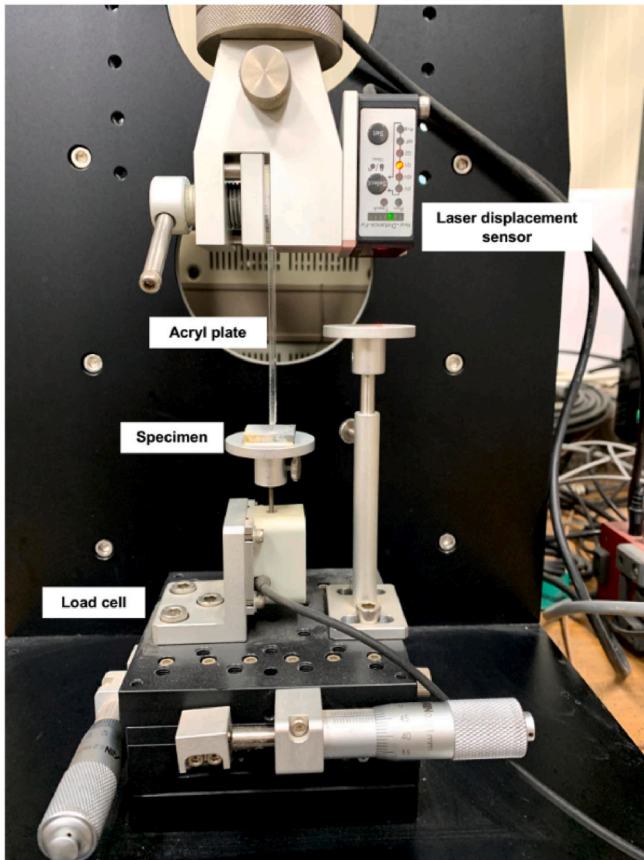
Fig. 4 presents the compressive strength ( $f_c$ ) and hardened density ( $\rho_h$ ) of each mixture at 28 days of age. In general, higher SMP/SH ratio resulted in lower density. The UD-EGC20 mixture showed the lowest  $\rho_h$  of  $1.44 \text{ g/cm}^3$ , lower than those of the UD-EGC10 and UD-EGC15 mixtures by 21.4% and 13.2%, respectively. This trend is likely due to increase in porosity of UD-EGC caused by the increase in crystalline SMP particles. Even though the SMP particles were completely dissolved in the pretreatment stage, the particles were likely reformed during the mixing process. The temperature to fully dissolve sodium silicate is  $150 \text{ }^\circ\text{C}$ – $160 \text{ }^\circ\text{C}$ , which is much higher than the temperature generated by

mixing NaOH with water (section 2.1) [37]. Therefore, during curing in the oven, hardened SMP particles might have increased the porosity of the geopolymer matrix, leading to a decrease in density. Fig. 5 presents a cross-section of the UD-EGC specimen showing millimeters-sized pores in the matrix. The UD-EGC mixtures studied show density values lower than the upper bound of lightweight concrete ( $1.92 \text{ g/cm}^3$  [38,39]).

Although the porosity increased with increasing SMP/SH ratio,  $f_c$  increased with the increase in the SMP/SH ratio from 1 to 2. The  $f_c$  of the UD-EGC20 mixture was 22.4 MPa, which was higher than those of the UD-EGC10 and UD-EGC15 mixtures by 42.6% and 16.1%, respectively. According to past studies, an increase of SMP/SH ratio promoted the geopolymerization rate, inducing higher  $f_c$  [40,41]. It seems that  $f_c$  was more significantly influenced by the geopolymerization rate than by the porosity. However, once the SMP/SH ratio exceeded 2,  $f_c$  decreased



(a)



(b)

Fig. 3. Fiber pullout test showing (a) specimen configuration and (b) test set-up.

because excessive alkali content retarded the geopolymerization reaction. As a result,  $f_c$  of the UD-EGC25 mixture was 27.6% lower than that of the UD-EGC20 mixture. According to the ACI 318 Code [42], a minimum specified compressive strength for structural concrete is 2500 psi, corresponding to 17.2 MPa. The UD-EGC15 and UD-EGC20 mixtures satisfied the requirement.

### 3.2. Tensile behavior

Fig. 6 shows the tensile stress-strain curves of the UD-EGC mixtures at 28 days of age. All mixtures showed the pseudo strain-hardening and

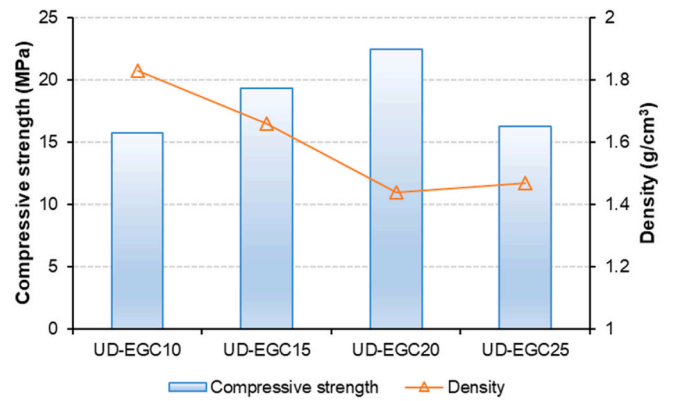


Fig. 4. Compressive strength and density of UD-EGC mixtures.

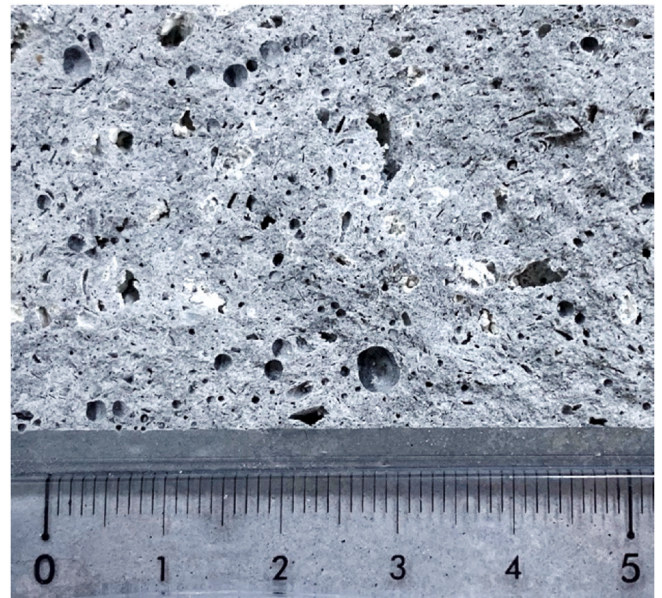
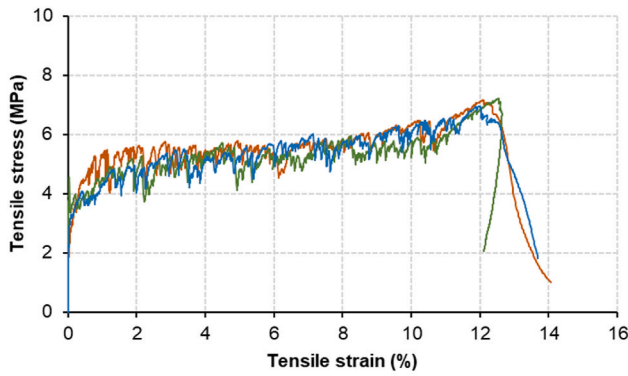


Fig. 5. Cross section of UD-EGC20 specimen (scale unit: cm).

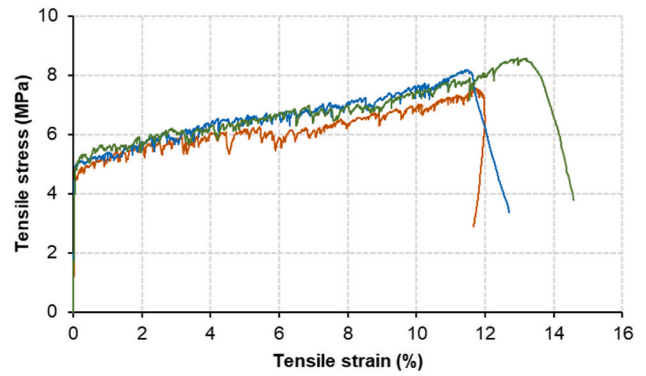
multiple cracking behavior similar to ECC. Stress fluctuations after the first cracking were observed until the peak stress (tensile strength); each stress drop indicates the occurrence of a new crack. The stress-strain curves of the three specimens of each mixture were similar, indicating the repeatability of the test results. Interestingly, all mixtures exhibited ultra-ductile behavior with tensile strain capacity of over 10%. The first cracking strength ( $f_{cr}$ ), tensile strength ( $f_{ts}$ ), tensile strain capacity ( $\epsilon_{ts}$ ), and toughness ( $E_t$ ) are summarized in Table 4.

The tensile stress-strain curves for all mixtures can be represented using a trilinear model as shown in Fig. 7. The strain-hardening criteria of UD-EGC mixtures was apparently satisfied as  $f_{ts}$  was higher than  $f_{cr}$  for all mixtures [43,44]. In general,  $f_{cr}$  increased with a rise of the SMP/SH ratio. Specifically, the  $f_{cr}$  of UD-EGC25 was 2.34, 1.35, and 1.08 times that of the UD-EGC10, UD-EGC15, and UD-EGC20 mixtures, respectively. Similar to  $f_{cr}$ ,  $f_{ts}$  also increased with increase in SMP/SH ratio, although there was a slight decrease in  $f_{ts}$  when the SMP/SH ratio exceeded 2.0.

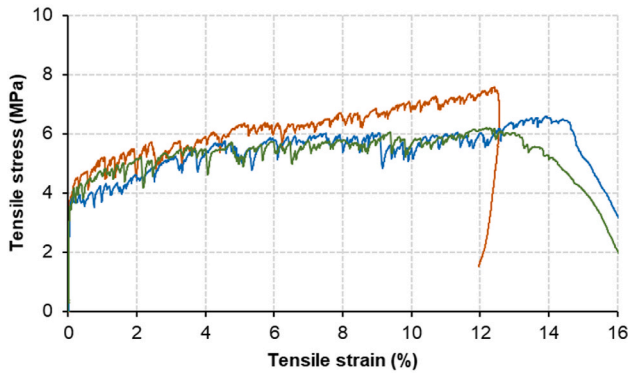
In terms of  $\epsilon_{ts}$ , the UD-EGC15 mixture showed the highest tensile strain capacity, with a remarkable  $E_t$ . Although  $E_t$  represents the ability



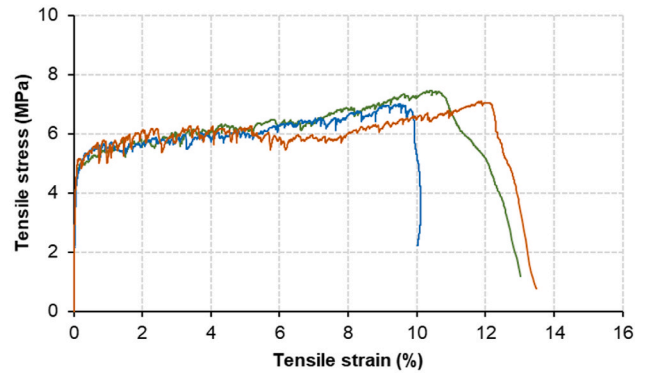
(a)



(c)



(b)



(d)

Fig. 6. Tensile behavior of: (a) UD-EGC10, (b) UD-EGC15, (c) UD-EGC20, and (d) UD-EGC25 mixtures.

Table 4  
Tensile properties of UD-EGC mixtures.

Mixture	$f_{cr}$ (MPa)	$f_{ts}$ (MPa)	$\epsilon_{ts}$ (%)	$E_t$ (MPa m/m)
UD-EGC10	$2.13 \pm 0.14$	$7.11 \pm 0.11$	$12.49 \pm 0.09$	0.58
UD-EGC15	$3.70 \pm 0.11$	$6.79 \pm 0.58$	$13.68 \pm 0.85$	0.71
UD-EGC20	$4.63 \pm 0.26$	$8.10 \pm 0.42$	$12.26 \pm 0.71$	0.78
UD-EGC25	$4.99 \pm 0.34$	$7.18 \pm 0.21$	$10.88 \pm 0.93$	0.66

Table 5  
Tensile strength-to-compressive strength ratios of UD-EGC mixtures.

Mixtures	$f_{ts}/f_c$ (%)
UD-EGC10	45.2
UD-EGC15	35.1
UD-EGC20	36.1
UD-EGC25	44.2

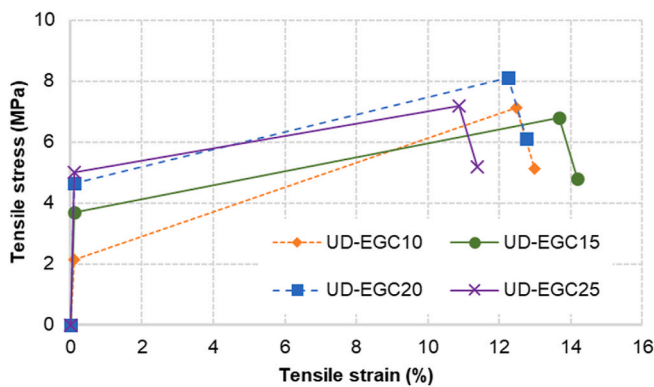


Fig. 7. Comparison of tensile performance of each UD-EGC mixture.

to absorb energy under quasi-static tensile load, it is also a measure of the tensile strain capacity of composites reinforced by synthetic fibers. In general, higher  $\epsilon_{ts}$  led to higher  $E_t$ . The UD-EGC15 and UD-EGC20 mixtures achieved relatively higher values of  $\epsilon_{ts}$  and  $E_t$ .  $\epsilon_{ts}$  of the UD-EGC15 mixture was higher than that of the UD-EGC10, UD-EGC20, and UD-EGC25, by 9.5%, 11.6%, and 25.7%, respectively. Thus, the tensile strain capacity of the UD-EGC mixtures increased with increase in SMP/SH ratio from 1.0 to 1.5, but then decreased for SMP/SH ratio greater than 1.5. A likely explanation for this observation is that the higher amount of sodium silicate pentahydrate induced excessive bonding between the matrix and the reinforcing fiber, leading to a lower tensile strain capacity. Micromechanical analysis is adopted in the next section to explain this further.

Table 5 lists the tensile strength-to-compressive strength ratio of the mixtures. The stress ratio of conventional concrete is approximately 10%. The stress ratios of UD-EGC mixtures are higher than those of normal concrete by 3.5–4.5 times, indicating the great potential of UD-

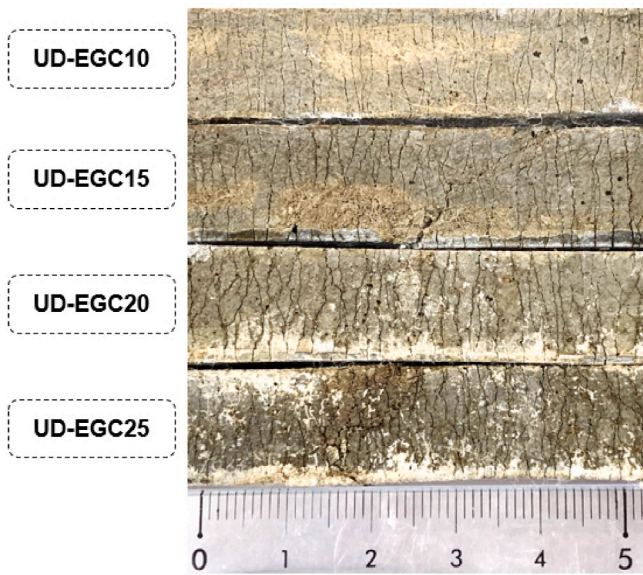


Fig. 8. Observed cracking patterns of UD-EGC mixtures.

Table 6  
Cracking patterns of UD-EGC mixtures.

Mixtures	$\eta_c$	$l_s$ (mm)	$\omega_c$ ( $\mu\text{m}$ )
UD-EGC10	65.3 $\pm$ 2.4	1.18 $\pm$ 0.04	147.5 $\pm$ 5.8
UD-EGC15	77.5 $\pm$ 4.7	1.00 $\pm$ 0.06	136.7 $\pm$ 14.8
UD-EGC20	73.8 $\pm$ 6.9	1.09 $\pm$ 0.09	132.7 $\pm$ 4.3
UD-EGC25	62.2 $\pm$ 5.4	1.21 $\pm$ 0.11	131.3 $\pm$ 12.6

Table 7  
Matrix properties and interfacial properties of UD-EGC15 and UD-EGC20 mixtures.

Mixture	$K_m$ (MPa $\text{m}^{1/2}$ )	$E_m$ (GPa)	$J_{ip}$	$\tau_0$ (MPa)	$\beta$
UD-EGC15	0.07 $\pm$ 0.00	8.29 $\pm$ 0.41	0.57 $\pm$ 0.07	0.55 $\pm$ 0.14	-0.0127 $\pm$ 0.0055
UD-EGC20	0.11 $\pm$ 0.01	9.35 $\pm$ 0.18	1.26 $\pm$ 0.30	0.63 $\pm$ 0.11	-0.0008 $\pm$ 0.0009

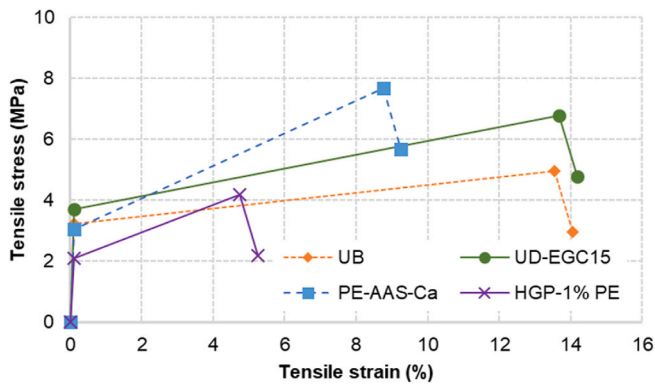


Fig. 9. Tensile stress-strain behavior of UD-EGC15 mixture and those of previous studies.

EGC mixtures to enhance structural performance in term of tensile behavior. It is rare for an inorganic composite to have  $f_{ts}$  close to 50% of its  $f_c$ . In fact,  $f_c$  is usually seen as a performance indicator in structural design. However, for UD-EGC,  $f_{ts}$  may serve as an indicator of performance of composite structures.

Fig. 8 shows the cracking patterns of the UD-EGC mixtures, which are quantified by crack number ( $\eta_c$ ), crack spacing ( $l_s$ ), and average crack width ( $\omega_c$ ), as shown in Table 6. Fig. 8 shows the multiple cracks along a length of 5 cm.  $\eta_c$  of the UD-EGC15 mixture, which showed the highest tensile stain capacity, was higher than that of the UD-EGC10, UD-EGC20, and UD-EGC25 mixtures by 18.6%, 5.4%, and 24.6%, respectively.  $l_s$  of all mixtures ranged from 1.00 mm to 1.21 mm, suggesting saturated crack patterns.  $\omega_c$  values are in a range of 131  $\mu\text{m}$ –148  $\mu\text{m}$ . These values are approximately two times higher than those (55  $\mu\text{m}$ –67  $\mu\text{m}$ ) of ultra-ductile behavior alkali-activated slag based composites [43] but slightly smaller than those (121  $\mu\text{m}$ –288  $\mu\text{m}$ ) of the ultra-ductile ECC [30]. The main reason for the high value of  $\omega_c$  is likely related to a lower fiber/matrix bond in the present compositions.

Fig. 9 compares the tensile behavior of the UD-EGC15 mixture with that of fly ash and slag blended geopolymer composites in the literature. The PE-AAS-Ca [43], UB [45], and UD-EGC15 mixtures showed similar values of  $f_{cr}$ , whereas the  $f_{cr}$  of the HGP-1% PE mixture [27] was two-third of  $f_{cr}$  of the other three mixtures. The  $f_{ts}$  of the UD-EGC15 mixture was higher than that of the HGP-1% PE and UB mixtures by 61.7% and 36.6%, respectively, but lower than that of the PE-AAS-Ca mixture by 11.5%. Interestingly,  $\epsilon_{ts}$  of the UD-EGC15 mixture was higher than that of the HGP-1% PE, PE-AAS-Ca, and UB mixtures by 188%, 56.3%, and 0.96%, respectively. Overall, the UD-EGC15 mixture showed outstanding tensile properties compared to the other mixtures reported in the literature. According to the ISO 6935–2, the tensile strain capacity of the C-class steel used for reinforcing concrete should be higher than 7% at maximum force and 14% at fracture [46]. Hence, it can be seen that the tensile strain capacity of the UD-EGC15 mixture meets these requirements.

### 3.3. Micromechanical analysis

According to micromechanical theory, strength-based and energy-based criteria must be satisfied to facilitate pseudo strain-hardening behavior in fiber-reinforced brittle matrix composites [47,48]. Specifically, the strength and energy criteria can be expressed as shown in Equations (2) and (3).

$$\sigma_{fc} \leq \min(\sigma_0) \tag{2}$$

$$J_{ip} \leq \sigma_0 \delta_0 - \int_0^{\delta_0} \sigma(\delta) d\delta = J'_b \tag{3}$$

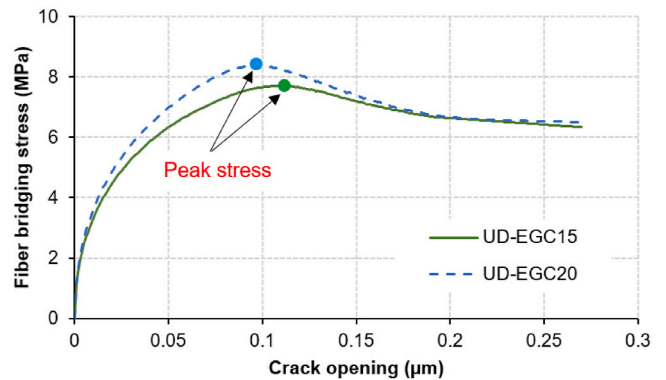
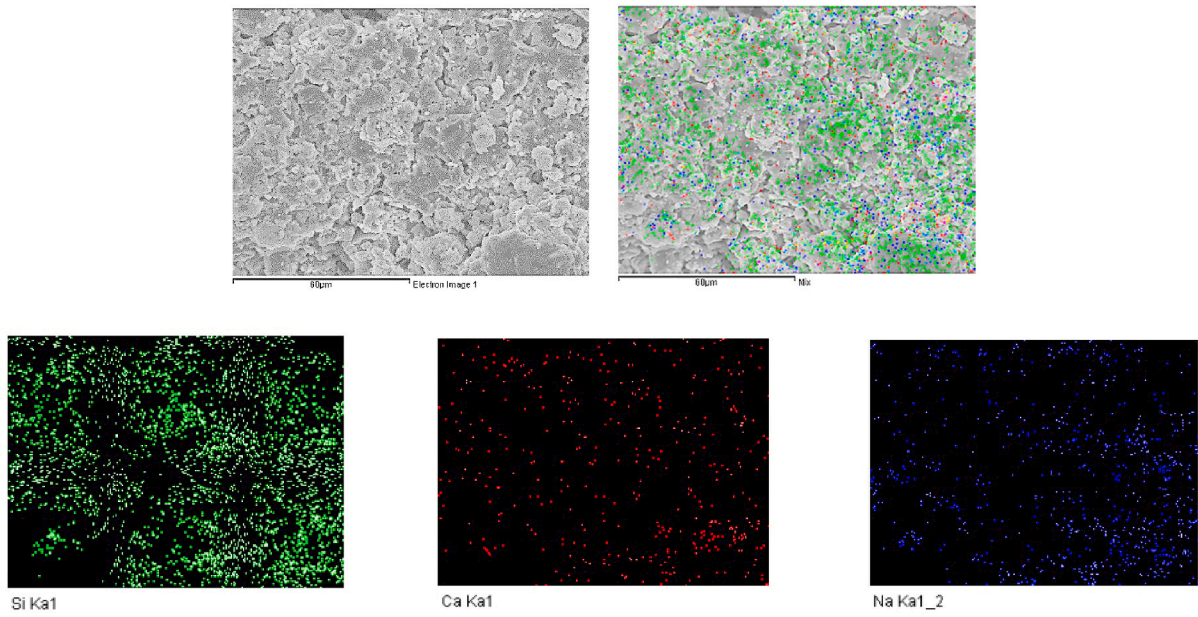
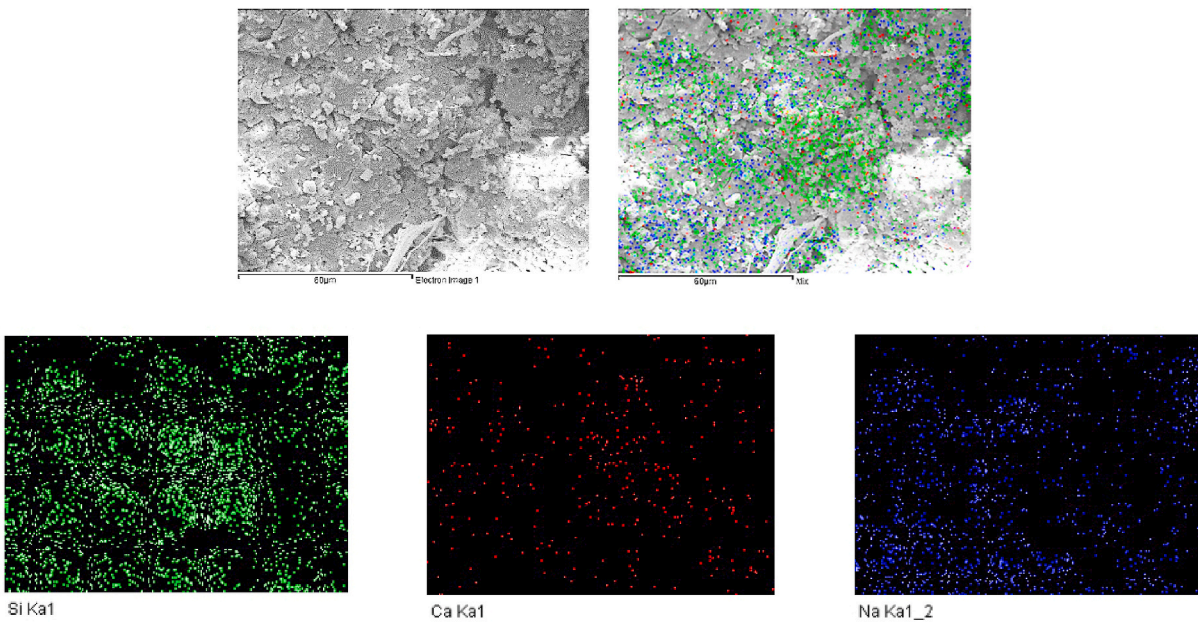


Fig. 10. Computed fiber-bridging curves of UD-EGC15 and UD-EGC20 mixtures.



(a)



(b)

Fig. 11. Microstructural characterization of: (a) UD-EGC15 and (b) UD-EGC20 mixtures.

**Table 8**  
Computed information on micromechanical properties of UD-EGC15 and UD-EGC20 mixtures.

Mixture	$\sigma_0$ (MPa)	$\delta_0$ ( $\mu\text{m}$ )	$J_b'$ ( $\text{J}/\text{m}^2$ )
UD-EGC15	7.71	107.10	184.03
UD-EGC20	8.37	95.40	191.20

**Table 9**  
Chemical compositions of UD-EGC matrices.

Mixture	Element	C	O	Na	Al	Si	Ca
UD-EGC15	Atomic (%)	24.86	41.75	6.43	3.49	21.21	2.26
UD-EGC20	Atomic (%)	26.82	42.93	9.36	3.16	16.51	1.22

where  $\sigma_{fc}$  is the first cracking strength and  $\min(\sigma_0)$  is the bridging capacity of the least bridged crack. Due to non-homogeneous fiber dispersion, each crack has a different bridging capacity ( $\sigma_0$ ). In a multiple cracking process,  $\min(\sigma_0)$  is the minimum of the bridging capacities among all the cracks formed until the next crack formation.  $J_{tip}$  is approximated as the crack tip toughness of the matrix and  $J_b'$  is the complementary energy of fiber bridging [47,48].

The strength-based criterion of UD-EGC was satisfied, as demonstrated in Section 3.2. The stress performance index ( $PSH_s$ ) is defined by  $\sigma_0/\sigma_{fc}$  [47].  $PSH_s$  values of the UD-EGC15 and UD-EGC20 mixtures, which showed relatively high tensile behavior in terms of tensile strength and tensile strain capacity, were 1.84 and 1.75, respectively.

$J_b'$  was obtained from the fiber bridging stress-crack opening ( $\sigma-\delta$ ),

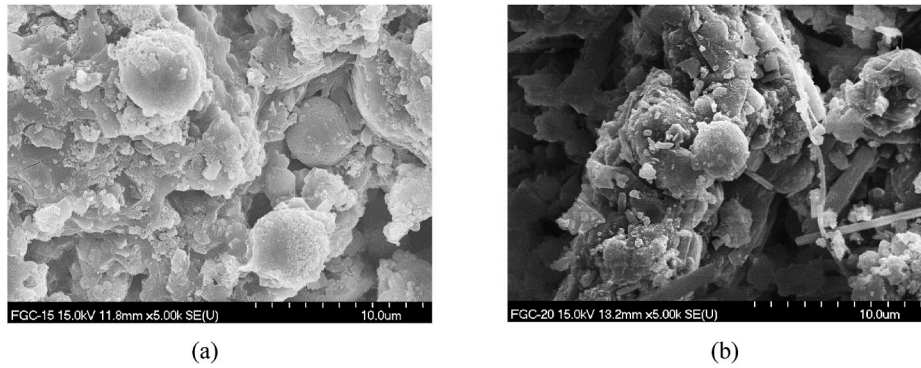


**Fig. 12.** Matrix with un-hydrated fly ash of: (a) UD-EGC15 and (b) UD-EGC20 mixtures.

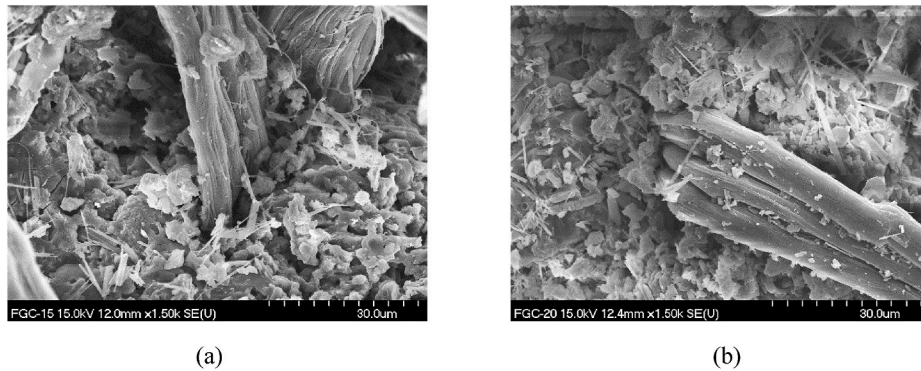


**Fig. 13.** Morphology of PE fiber embedded in matrix of: (a) UD-EGC15 and (b) UD-EGC20 mixtures.

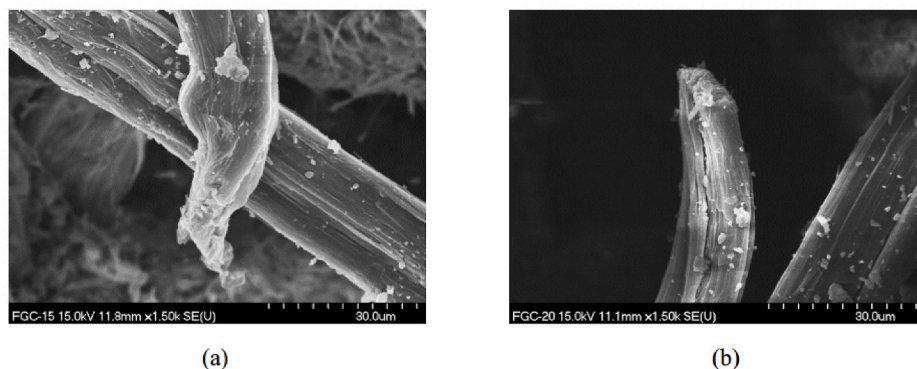


**Fig. 14.** Morphology of fractured PE fiber pulled out from: (a) UD-EGC15 and (b) UD-EGC20 mixtures.

while  $J_{tip}$  was obtained from the matrix fracture toughness ( $K_m$ ) and elastic modulus ( $E_m$ ) through the ratio  $K_m^2/E_m$ .  $K_m$  was obtained from Equation (4), according to Ref. [49].

$$K_m = \frac{1.5P_{max}S\sqrt{\pi\alpha}}{BW^2} \left( \frac{0.68 - 0.744\alpha}{1 - 2.155\alpha + 1.161\alpha^2} + 0.36 - 2.088\alpha + 4.611\alpha^2 - 6.499\alpha^3 + 4.232\alpha^4 \right) \quad (4)$$

where  $B$  and  $W$  are the thickness and height of the notched beam (Fig. 2), respectively.  $\alpha$  is the relative notch depth ratio to the beam height.

The interfacial properties, i.e. frictional bonding strength ( $\tau_0$ ) and strain-hardening coefficient ( $\beta$ ), were calculated from the single fiber pullout curves using Equation (5) to Equation (7) [36].

$$G_d = \frac{2(P_a - P_b)^2}{\pi^2 E_f d_f^3} \quad (5)$$

$$\tau_0 = \frac{P_b}{\pi d_f L_e} \quad (6)$$

$$\beta = \frac{d_f}{L_e} \left[ \left( \frac{1}{\tau_0 \pi d_f} \right) \left( \frac{\Delta P}{\Delta S} \right)_{\Delta S=0} + 1 \right] \quad (7)$$

Here  $E_f$ ,  $d_f$ , and  $L_e$  are the elastic modulus, diameter, and embedded length of PE fiber, respectively.  $\Delta P/\Delta S$  represents the initial slope between the pullout load and pullout distance.

Table 7 lists the values of  $K_m$ ,  $E_m$ ,  $J_{tip}$ ,  $\tau_0$ , and  $\beta$  for the two best-performing UD-EGCs, i.e., UD-EGC15 and UD-EGC20 mixtures at 28 days of age.  $E_m$  was obtained from the initial slope of the tensile stress versus strain curves, as shown in Fig. 6. Overall, UD-EGC20, which has higher strength than UD-EGC15, showed higher fracture toughness of matrix and frictional bond strength than those of UD-EGC15.

Based on the micromechanical parameters, theoretical fiber-bridging analysis was performed to get further insights into the tensile behavior of the UD-EGCs investigated in this study. Theoretical fiber-bridging curves were obtained from the fiber-bridging constitutive law [50,51]. The fiber strength reduction value, snubbing coefficient, and spalling coefficient used for the computation were obtained from past studies, with values of 0.475, 0.3, and 500, respectively [50,52,53]. Fig. 10 shows the simulated fiber-bridging curves of the two best-performing UD-EGCs.

Table 8 lists the peak bridging stress ( $\sigma_0$ ), maximum crack opening ( $\delta_0$ ), and complementary energy ( $J_b$ ), obtained from the theoretical fiber-bridging curves. Specifically,  $\sigma_0$  of the UD-EGC20 mixture was higher than that of the UD-EGC15 mixture by 8.4%. It can be confirmed that steady-state flat cracking was achieved as  $J_b > J_{tip}$ . Moreover, based on  $J_b$ , energy performance indexes ( $PSH_E$ ) of UD-EGC15 and UD-EGC20 were obtained through the ratio  $J_b/J_{tip}$ .  $PSH_E$  of the UD-EGC15 mixture was 322, which is 2.12 times higher than that of the UD-EGC20 mixture.

### 3.4. Microstructure analysis

Fig. 11(a) and (b) utilized a map of elements of the UD-EGC mixtures instead of a spectrum picked up at a certain position because EDS mapping was able to scan whole sections of the matrix. The chemical components are listed in Table 9. As expected, elemental Si was dominant due to the high amount of  $SiO_2$  contained in fly ash and SMP. Based on the percentages of atomic elements, it is likely that calcium-(sodium) aluminosilicate hydrate (C-(N)-A-S-H) and sodium aluminosilicate hydrate (N-A-S-H) were the major geopolymeric products. Furthermore, unhydrated fly ash particles were detected in the matrix (Fig. 12) which

may explain the observed modest  $f_c$  of the UD-EGC mixtures. It is proposed that the SMP was not as reactive as traditional sodium silicate, leading to an incomplete activation between fly ash particles and alkali

activators during the geopolymerization process.

Fig. 13 shows the fiber embedded in the matrix, whereas Fig. 14 displays the morphology of a fractured fiber pulled out from the two UD-EGC mixtures. As observed in these figures, the PE fibers were robustly bonded to the matrix material, contributing to the achievement of excellent tensile behavior. Needle-like crystals can be found at several positions around the PE fiber and matrix. Based on this morphology, the presence of ettringite was observed. As reported previously, massive amounts of secondary ettringite (delayed ettringite formation) are frequently detected when specimens are cured above 70 °C [54]. The pencil-tip shape of the fiber end suggests that the PE fiber ruptured during the crack opening process (Fig. 14).

## 4. Conclusions

In this research, meso- and micro-scale characterization of ultra-ductile fly ash-based engineered geopolymer composites (UD-EGC) was presented. The composite density, compressive strength, and tensile performance measurement were characterized. Micromechanical and chemical analyses were conducted to further understand the mechanical properties and ultra-ductile behavior of these composites. The following conclusions can be drawn:

1. The compressive strength of UD-EGC mixtures increased with increase in the SMP/SH ratio. However, the compressive strength dropped when this ratio exceeded 2.0. The maximum compressive strength was 22.4 MPa, achieved for the UD-EGC20 mixture.
2. All UD-EGC mixtures were lightweight with density below 1.83 g/cm<sup>3</sup>. The density tended to decrease with increase in the SMP/SH ratio, at least up to SMP/SH = 2.0.
3. All mixtures reached tensile strain capacity over 10%. UD-EGC15 attained a remarkable tensile strain capacity of 13.7% and a tensile strength of 6.8 MPa at 28 days of age. These properties are higher than those of fly ash-based engineered geopolymer composites as well as engineered cementitious composites reported in the literature.
4. The observed ultra-ductile behavior of UD-EGC is supported by micromechanical analyses. Specifically, the stress and energy performance indices of the best-performing UD-EGC15 mixture were 1.84 and 322, respectively, significantly greater than that required for robust strain-hardening with saturated multiple cracking.
5. Chemical analyses revealed the presence of C-(N)-A-S-H and N-A-S-H as dominant geopolymeric products. Unhydrated fly ash particles were observed after the geopolymerization process. Ettringite, likely formed as a result of high curing temperature, was identified through its typical morphology of needle-like crystals.

## Declaration of competing interest

The authors declare that they have no known competing financial interests or personal relationships that could have appeared to influence the work reported in this paper.

## Acknowledgements

This work was supported by the National Research Foundation of Korea (NRF) grant funded by the Korea government (MSIT) (No. 2019R1A2C4069794).

## References

- [1] V.C. Li, On engineered cementitious composites (ECC), *J. Adv. Concr. Technol.* 1 (3) (2003) 215–230.
- [2] V.C. Li, S. Wang, C. Wu, Tensile strain-hardening behavior of polyvinyl alcohol engineered cementitious composite (PVA-ECC), *ACI Mater. J.* 98 (6) (2001) 483–492.
- [3] M.D. Lepech, V.C. Li, Water permeability of engineered cementitious composites, *Cement Concr. Compos.* 31 (10) (2009) 744–753.
- [4] R. Ranade, V.C. Li, M.D. Stults, W.F. Heard, T.S. Rushing, Composite properties of high-strength, high-ductility concrete, *ACI Mater. J.* 110 (4) (2013) 413–422.
- [5] V. Malhotra, Introduction: sustainable development and concrete technology, *Concr. Int.* 24 (7) (2002) 22.
- [6] B. Nematollahi, J. Qiu, E.-H. Yang, J. Sanjayan, Microscale investigation of fiber-matrix interface properties of strain-hardening geopolymer composite, *Ceram. Int.* 43 (17) (2017) 15616–15625.
- [7] J.-I. Choi, B.Y. Lee, R. Ranade, V.C. Li, Y. Lee, Ultra-high-ductile behavior of a polyethylene fiber-reinforced alkali-activated slag-based composite, *Cement Concr. Compos.* 70 (2016) 153–158.
- [8] J.-I. Choi, S.-E. Park, H.H. Nguyễn, S.L. Cha, B.Y. Lee, Strain-hardening and high-ductile behavior of alkali-activated slag-based composites with added zirconia silica fume, *Materials* 12 (21) (2019) 3523.
- [9] R. Pierrehumbert, There is no Plan B for dealing with the climate crisis, *Bull. At. Sci.* 75 (5) (2019) 215–221.
- [10] G. Fayomi, S. Mini, O. Fayomi, A. Ayoola, Perspectives on Environmental CO<sub>2</sub> Emission and Energy Factor in Cement Industry, IOP Conference Series: Earth and Environmental Science, IOP Publishing, 2019, 012035.
- [11] J.G. Olivier, J.A. Peters, report Trends in Global CO<sub>2</sub> and Total Greenhouse Gas Emissions: 2017 Report, PBL Netherlands Environmental Assessment Agency The Hague 2017.
- [12] Q.-H. Lương, H.H. Nguyễn, J.-I. Choi, H.-K. Kim, B.Y. Lee, Effects of crumb rubber particles on mechanical properties and sustainability of ultra-high-ductile slag-based composites, *Construct. Build. Mater.* 272 (2021), 121959.
- [13] Á. Palomo, E. Kavalerova, A. Fernández-Jiménez, P. Krivenko, I. García-Lodeiro, O. Maltseva, A Review on Alkaline Activation: New Analytical Perspectives, 2015.
- [14] J.L. Provis, Geopolymers and other alkali activated materials: why, how, and what? *Mater. Struct.* 47 (1) (2014) 11–25.
- [15] C. Ouellet-Plamondon, G. Habert, Life Cycle Assessment (LCA) of Alkali-Activated Cements and Concretes, *Handbook of Alkali-Activated Cements, Mortars and Concretes*, Elsevier 2015, pp. 663–686.
- [16] J.L. Provis, J.S.J. Van Deventer, *Geopolymers: Structures, Processing, Properties and Industrial Applications*, Elsevier 2009.
- [17] X. Li, Z. Wang, Z. Jiao, Influence of curing on the strength development of calcium-containing geopolymer mortar, *Materials* 6 (11) (2013) 5069–5076.
- [18] G. Kastiukas, S. Ruan, S. Liang, X. Zhou, Development of precast geopolymer concrete via oven and microwave radiation curing with an environmental assessment, *J. Clean. Prod.* 255 (2020), 120290.
- [19] S. Pilehvar, S.G. Sanfelix, A.M. Szczotok, J.F. Rodríguez, L. Valentini, M. Lanzón, R. Pamies, A.-L. Kjøniksen, Effect of temperature on geopolymer and Portland cement composites modified with Micro-encapsulated Phase Change materials, *Construct. Build. Mater.* 252 (2020), 119055.
- [20] J. Davidovits, Green chemistry and sustainable development solutions, *Proc. World Congr. Geopolym.* (2005) 9–15.
- [21] B. Nematollahi, J. Sanjayan, F.U.A. Shaikh, Matrix design of strain hardening fiber reinforced engineered geopolymer composite, *Compos. B Eng.* 89 (2016) 253–265.
- [22] Y. Liu, Z. Zhang, C. Shi, D. Zhu, N. Li, Y. Deng, Development of ultra-high performance geopolymer concrete (UHPGC): influence of steel fiber on mechanical properties, *Cement Concr. Compos.* 112 (2020), 103670.
- [23] N. Ranjbar, M. Mehrali, M. Mehrali, U.J. Alengaram, M.Z. Jumaat, High tensile strength fly ash based geopolymer composite using copper coated micro steel fiber, *Construct. Build. Mater.* 112 (2016) 629–638.
- [24] B. Nematollahi, J. Sanjayan, F.U.A. Shaikh, Comparative deflection hardening behavior of short fiber reinforced geopolymer composites, *Construct. Build. Mater.* 70 (2014) 54–64.
- [25] M.M. Al-Mashhadani, O. Canpolat, Y. Ayygörmöz, M. Uysal, S. Erdem, Mechanical and microstructural characterization of fiber reinforced fly ash based geopolymer composites, *Construct. Build. Mater.* 167 (2018) 505–513.
- [26] B. Nematollahi, J. Sanjayan, J. Qiu, E.-H. Yang, High ductile behavior of a polyethylene fiber-reinforced one-part geopolymer composite: a micromechanics-based investigation, *Arch. Civil Mech. Eng.* 17 (3) (2017) 555–563.
- [27] F.U.A. Shaikh, A. Fairchild, R. Zammam, Comparative strain and deflection hardening behaviour of polyethylene fibre reinforced ambient air and heat cured geopolymer composites, *Construct. Build. Mater.* 163 (2018) 890–900.
- [28] Y. Ding, J.-t. Yu, K.-Q. Yu, S.-l. Xu, Basic mechanical properties of ultra-high ductility cementitious composites: from 40 MPa to 120 MPa, *Compos. Struct.* 185 (2018) 634–645.
- [29] K.-Q. Yu, J.-T. Yu, J.-G. Dai, Z.-D. Lu, S.P. Shah, Development of ultra-high performance engineered cementitious composites using polyethylene (PE) fibers, *Construct. Build. Mater.* 158 (2018) 217–227.
- [30] L. Li, Z. Cai, K. Yu, Y. Zhang, Y. Ding, Performance-based design of all-grade strain hardening cementitious composites with compressive strengths from 40 MPa to 120 MPa, *Cement Concr. Compos.* 97 (2019) 202–217.
- [31] K.-Q. Yu, J.-G. Dai, Z.-D. Lu, C.-S. Poon, Rate-dependent tensile properties of ultra-high performance engineered cementitious composites (UHP-ECC), *Cement Concr. Compos.* 93 (2018) 218–234.
- [32] K. Yu, Y. Wang, J. Yu, S. Xu, A strain-hardening cementitious composites with the tensile capacity up to 8%, *Construct. Build. Mater.* 137 (2017) 410–419.
- [33] ASTM, Standard Test Method for Compressive Strength of Hydraulic Cement Mortars (Using 2-in. Or [50-mm] Cube Specimens), ASTM C109/C109M-07, American Society for Testing and Materials, ASTM International West, Conshohocken, PA, 2007.
- [34] JSCE, Recommendations for Design and Construction of High Performance Fiber Reinforced Cement Composites with Multiple Fine Cracks (HPFRCC), Japan Society of Civil Engineers, Japan, 2008.
- [35] ASTM, Standard Test Method for Linear-Elastic Plane-Strain Fracture Toughness K<sub>IC</sub> of Metallic Materials, American Society for Testing and Materials, ASTM International West, Conshohocken, PA, 2012.
- [36] C. Redon, V.C. Li, C. Wu, H. Hoshiro, T. Saito, A. Ogawa, Measuring and modifying interface properties of PVA fibers in ECC matrix, *J. Mater. Civ. Eng.* 13 (6) (2001) 399–406.
- [37] U. (Umweltbundesamt, German Notes on BAT of the Production of Large Volume Solid Inorganic Chemicals: Sodium Silicate, UBA (Umweltbundesamt), 2001.
- [38] D.J. Akers, R.D. Gruber, B.W. Ramme, M.J. Boyle, J.G. Grygar, S.K. Rowe, T. W. Bremner, E.S. Kluckowski, S.R. Sheetz, R.G. Burg, Guide for Structural Lightweight-Aggregate Concrete, ACI 213R-03, American Concrete Institute (ACI), Michigan, 2003.
- [39] Z. Zhang, A. Yuvaraj, J. Di, S. Qian, Matrix design of light weight, high strength, high ductility ECC, *Construct. Build. Mater.* 210 (2019) 188–197.
- [40] Z. Yahya, M.M.A.B. Abdullah, K. Hussin, K.N. Ismail, R.A. Razak, A.V. Sandu, Effect of solids-to-liquids, Na<sub>2</sub>SiO<sub>3</sub>-to-NaOH and curing temperature on the palm oil boiler ash (Si+ Ca) geopolymerisation system, *Materials* 8 (5) (2015) 2227–2242.
- [41] D. Hardjito, S.E. Wallah, D.M. Sumajouw, B.V. Rangan, Fly ash-based geopolymer concrete, *Aust. J. Struct. Eng.* 6 (1) (2005) 77–86.
- [42] ACI Committee 318, Building Code Requirements for Structural Concrete (ACI 318-14) and Commentary (ACI 318R-14), American Concrete Institute, Farmington Hills, MI, 2014.
- [43] H.H. Nguyễn, J.-I. Choi, H.-K. Kim, B.Y. Lee, Mechanical properties and self-healing capacity of eco-friendly ultra-high ductile fiber-reinforced slag-based composites, *Compos. Struct.* 229 (2019), 111401.
- [44] S.-J. Kwon, J.-I. Choi, H.H. Nguyễn, B.Y. Lee, Tensile strain-hardening behaviors and crack patterns of slag-based fiber-reinforced composites, *Comput. Concr.* 21 (3) (2018) 231–237.
- [45] K. Yu, L. Li, J. Yu, J. Xiao, J. Ye, Y. Wang, Feasibility of using ultra-high ductility cementitious composites for concrete structures without steel rebar, *Eng. Struct.* 170 (2018) 11–20.
- [46] ISO 6935-2, Steel for the Reinforcement of Concrete – Part 2: Ribbed Bars, International Organization for Standardization, Geneva, 2019.
- [47] T. Kanda, V.C. Li, Practical design criteria for saturated pseudo strain hardening behavior in ECC, *J. Adv. Concr. Technol.* 4 (1) (2006) 59–72.
- [48] V.C. Li, C.K. Leung, Steady-state and multiple cracking of short random fiber composites, *J. Eng. Mech.* 118 (11) (1992) 2246–2264.
- [49] S. Zhang, V.C. Li, G. Ye, Micromechanics-guided development of a slag/fly ash-based strain-hardening geopolymer composite, *Cement Concr. Compos.* 109 (2020), 103510.
- [50] E.-H. Yang, S. Wang, Y. Yang, V.C. Li, Fiber-bridging constitutive law of engineered cementitious composites, *J. Adv. Concr. Technol.* 6 (1) (2008) 181–193.
- [51] J.-I. Choi, H.-K. Kim, B.Y. Lee, Mechanical and fiber-bridging behavior of slag-based composite with high tensile ductility, *Appl. Sci.* 10 (12) (2020) 4300.
- [52] J.-I. Choi, B.Y. Lee, Bonding properties of basalt fiber and strength reduction according to fiber orientation, *Materials* 8 (10) (2015) 6719–6727.
- [53] C. Wu, *Micromechanical Tailoring of PVA-ECC for Structural Applications*, 2001.
- [54] C. Maierhofer, H.-W. Reinhardt, G. Dobmann, *Non-destructive Evaluation of Reinforced Concrete Structures: Non-destructive Testing Methods*, Elsevier 2010.